Oxidation behavior of dense Yttrium doped B2-NiAl bulk material fabricated by ball milling self-propagating high-temperature synthesis and densified by spark plasma sintering

J. Muñoz-Saldaña[1,2,*], A. Valencia-Ramirez[1], L.A Castillo-Perea[1], S. Díaz-De la Torre[3], L.A. Caceres-Diaz[4], J. M. Alvarado Orozco[5], A. L. Giraldo Betancur[6], U. Schulz[2]

[1] Centro de Investigación y de Estudios Avanzados del IPN, Lib. Norponiente 2000, Fracc. Real de Juriquilla, 76230 Querétaro, Qro. México
[2] German Aerospace Center (DLR), Institute of Materials Research, Cologne, Germany.
[3] Centro de Investigación y de Innovación Tecnológica del IPN, México DF, México.
[4] CONACYT - CIATEQ A.C. Centro de Tecnología Avanzada, Eje 126 No.225, Industrial San Luis, San Luis Potosí 78395, Mexico.
[5] Centro de Ingeniería y Desarrollo Industrial, Av. Playa Pie de la Cuesta No. 702, Desarrollo San Pablo, Querétaro, C.P. 76125, México.
[6] CONACYT - Centro de Investigación y de Estudios Avanzados del IPN, Lib. Norponiente 2000, Fracc. Real de Juriquilla, 76230 Querétaro, Qro. México

https://doi.org/10.1016/j.surfcoat.2021.127448

Abstract

The effect of Y additions on the oxidation behavior in furnace cyclic tests and its correlation with thermogravimetric analysis of sintered NiAl alloys is here reported. Part of the samples got an EB-PVD 7YSZ coating on top. Highly ordered B2-NiAl intermetallic powder was obtained by self-propagating high-temperature synthesis (SHS) during ball milling of elemental precursors with Y additions in amounts between 0 and 1.5 at.%. The SHS process was optimized to identify the combination of milling parameters that leads to a sharp increase in the reaction temperature for intermetallic synthesis. The tested samples consisted of NiAl-Y buttons densified by spark plasma sintering (SPS). Furnace cyclic testing of the SPS-buttons at 1100 °C showed high resistance to spallation of the 7YSZ top-coat and a significant decrease in its oxide growth kinetics attributed to Y-additions. Contents below 0.5 at.% Y reduce the oxidation kinetics of NiAl exposed to thermal cycles at 1100 °C, while higher Y contents are favorable for a longer TBC life.

Keywords: NiAl intermetallic, self-propagating high temperature synthesis, spark plasma sintering, furnace cyclic tests.

* **Georg Forster** Humboldt fellow and corresponding author

1. Introduction

NiAl is an intermetallic compound of high technological interest and has been successfully used for aeronautical, aerospace, and energy generation applications taking advantage of its high melting point, low density, good thermal conductivity, and good oxidation and corrosion resistance [1,2].

NiAl alloy has a CsCl structure also known as B2 and is stable in a range of composition and a melting point of 1638 ^{o}C. The stoichiometric B2 phase consists of two interpenetrating cubic sublattices, each having the same number of sites and completely occupied by Al and Ni atoms (Ni)(Al). The quality or ordering of the B2 phase is described by the long-range order parameter *S*. The ordering is affected either by variations in its stoichiometry or its processing that includes synthesis and densification steps. Variations from stoichiometry are accommodated by the substitution of Ni atoms in Al sites in Ni-rich alloys and by the formation of vacancies on Ni sites in Al-rich compositions [1,3,4].

Preparation of bulk NiAl alloys from a combination of powder metallurgy and sintering processes has been previously described elsewhere under different terminologies such as self-propagating high-temperature synthesis (SHS), combustion synthesis, self-sustaining or self-propagating reactions, etc [5–8]. The synthesis of NiAl by SHS in high energy ball milling has been reported as a self-sustained reaction in individual particles accompanied by a large explosive energy release denoting the compound formation [6]. A key aspect of this process is to be able to *in-situ* monitoring the SHS process [5,7,8]. For instance, the phase formation kinetics of NiAl is very sensitive to the sample temperature and the atmosphere inside the vial. In the in-situ characterization during powder milling, an important step is to stop the process as soon as the reaction takes place to avoid deformations and changes in particle size or long-range ordering of the powder. Thus, high-energy ball milling is useful, not only been used to mix powder particles and controlling their particle size but also for the synthesis of equilibrium and metastable alloys [9,10].

Densification of NiAl powder can be achieved by several methods, including arc melting, spark plasma sintering (SPS), etc. In the latter, the short sintering times contribute to the microstructure conservation of the raw material with almost no grain coarsening effect, and most of all, high densification [11–13].

The advantage of having a method to prepare NiAl intermetallics from powder precursors relies on the fact that additions of different elements can be accurately controlled by monitoring solubility conditions in the synthesis process. Additions of reactive elements (RE) to NiAl such as Hf, La, Zr, Dy, Ce, or Y [14–28] have been proved to be an effective way to promote selective oxidation, reduction of the growth rate of transient oxide scales and inhibition of alumina scale failure leading to a positive effect on the lifetime of thermal barrier coatings (TBC) [16,21,29–33]. Successful dispersion of RE oxide plays a significant role to act as heterogeneous nucleation sites for the first formed oxides [16,34]. Under these conditions, the RE effect has been explained by the dynamic segregation theory [17,35].

RE solubility condition plays an important role in the microstructure and kinetic oxidation of the B2-NiAl system. The optimum content of Zr or Y for bulk NiAl alloys coatings for oxidation behavior has been reported to be between 0.05 to 0.08 at.% [33]. Additional aspects for TBC performance include the interplay between RE and elements diffusing from the superalloy into the BC, and changes in microstructure during cyclic loading, especially those affecting the thermally grown oxide (TGO) adherence.

Solubility conditions for Y in NiAl have been subject of discussion considering that this element presents a low solubility limit reported below 0.5 at.% [36] and in recent studies lower than 0.05 at.% of Y [37]. Yttrium additions to NiAl and NiAl containing bond coats reduce the oxidation rate, increase the scale adherence depending on its composition [38–40], and modify microstructural characteristics leading to sites for heterogeneous nucleation of the TGO, and avoid the growth of metastable oxides [41]. As a result, Y increases the adhesion properties on the BC/TGO/TC interfaces reducing the failure of the TBC system [38,40,42]. Finding the critical or optimum yttrium content in NiAl is crucial since all mentioned effects are quite sensitive to the RE content.

It is important to remark that Y has been found in oxide scales as elemental Y or Y_2O_3 particles as a consequence of the dynamic segregation across the grain boundaries leading in some cases to the formation of Yttrium Aluminum Garnet (YAG) compounds as a result of the reaction between Y_2O_3 and Al_2O_3. However, a detrimental effect on internal oxidation due to the low volume content of Y has not been reported yet [37,43].

The combination of powder metallurgy based on SHS and SPS sintering processes to obtain model alloys for the study of the standalone effect of RE-additions on the oxidation behavior of NiAl has been barely reported in the literature.

The effect of Y-doping on the oxidation behavior of NiAl can be tested either by weight gain measurements in the thermogravimetric analysis (TGA) or furnace cyclic testing (FCT), with or without top-coat deposits. The idea of carrying out the tests in fully densified bulk alloys is to isolate the outward diffusion effect of Y in concurrence to Al in the NiAl-Y alloy avoiding the interplay with other diffusing elements, e.g., from a superalloy.

In this work, the oxidation behavior, failure characteristics, and microstructure evolution of Y-doped NiAl buttons synthesized by the SHS method and sintered by SPS are presented and discussed after furnace cycle tests and thermogravimetric analysis. These model alloys were used to evaluate the effect of various Y doping levels in NiAl in both the sintered intermetallic condition and by adding a 7YSZ EB-PVD topcoat. The TBC samples emulate the conditions of Y doped NiAl bond coats having a TGO formed during the deposition of the TBC and further oxidation.

2. Experimental procedure

Commercial Ni (Spectrum chemical, 74 μm, 99.8 %), Al (Spectrum chemical, 44 - 400 μm, 99.8 %), and Y (Sigma Aldrich, 400 μm, 99.5 %) powders were mixed and milled in a SPEX 8000D using commercial WC vials and 10 mm balls. Experiments with NiAl stoichiometric ratios were carried out varying both numbers of balls (2, 3, and 5 balls) and a ball-to-powder ratio (BPR) (4:1, 6:1, and 10:1) to identify the optimal milling conditions for the B2 phase formation. Powder volumes (V1 to V4) were selected to fix the BPR and weighted inside a glovebox with an Ar atmosphere to avoid oxidations during the milling experiments. The vial temperature was real-time monitored fixing a thermocouple on its external wall until the SHS occurred which is also, indicative of the B2 intermetallic alloy phase formation. The instrumented vial with a fixed thermocouple allows the identification of the reaction (T_{reac}) and maximal temperatures (T_{max}) as well as the reaction time (t_{reac}). The milling process was stopped immediately after the identification of the temperature sharp increase. The compositions of the NiAl samples doped with Y up to 1.5 at.% are presented in Table 1.

Densification of the obtained alloys was carried out in a Spark plasma sintering (Dr Sinter SPS-1050) equipment in vacuum at 1200 °C by using a constant uniaxial pressure of 6 kN. The cooling stage was performed with a water flux at 25 ºC/min using a graphite die to have a uniform flux of both electrical and thermal conductivity. During the SPS process, the displacement was continuously monitored, matching the beginning of the compaction and sintering times. The obtained samples after this process were round-shaped buttons with a diameter and thickness of 10 and 4.5 mm, respectively.

The crystal structure and phase formation of the powders and sintered samples were determined by X-ray diffraction (XRD) using a Rigaku Dmax2100 diffractometer with CuKα radiation (λ=1.54 Å) operated at 40 kV and 20 mA. The XRD patterns were recorded in a 2θ range of 20 to 80 º and from 20 to 90 º with a step size of 0.02 º for both precursors and sintered samples, respectively. Rietveld refinements were used to identify the B2 phase formation and to calculate its lattice constant as a function of Y-content. Additionally, the long-range ordering parameter (*S*) was calculated using the intensities of the pattern for each sample according to Eq. 1 [44]:

$$S = \sqrt{\frac{(I_{100}/I_{110})_{obs}}{(I_{100}/I_{110})_{std}}} \qquad \text{(Eq 1)}$$

Where I_{hkl} *obs* are the intensities of the (100) and (110) planes that correspond to the super-lattice and fundamental reflections, respective to the JCPDF file standard (std).

The microstructure of sintered samples was recorded in a field emission scanning electron microscope Jeol JSM-7200F equipped with a Electron Backscattered Diffraction (EBSD) detector under an accelerating voltage of 20 kV.

Thermogravimetric analysis (TGA) of the sintered samples was carried out in a Setaram Setsys Evolution 16/18 thermo-balance at 1100 °C for 10 h in air (pO_2=0.2 atm). The weight gain was normalized respective to the oxidized area and reported as a function of time. The TGA samples were again characterized by XRD and SEM. Microstructural characterization of the powders was performed using Philips XL-30 SEM and the cross-section was measured using Zeiss ULTRA 55 SEM. A secondary electron detector and 6-15 kV accelerating voltage were used in both cases.

A standard columnar 7YSZ top-coat was deposited on samples from each Y-content by EB-PVD in a 150 kW coater (ESPRI). The substrate temperature was maintained between 980 and 1000 °C, and the oxygen flow into the coating chamber was controlled to reach pressure in the chamber between 6 to 8 x 10^{-3} mbar. Samples were rotated during deposition by 12 rpm and the deposition rate was around 5 μm/min. Subsequently, the samples were exposed under furnace cycle tests for 10 and 100 h or until the spallation occurred. One cycle consisted of a 50 min heating period followed by rapid cooling under forced air of 10 min according to the standard FCT-tests of DLR.

3. Results and Discussion

3.1 Starting powder

The most important factors defining the SHS conditions in the high energy milling process are associated with the characteristics of the starting powders including their morphology, size, and size distribution. SEM micrographs of a) Ni, b) Al, and c) Y powders are shown in Figure 1. The morphology of Ni is typical of powder produced by a hydrometallurgical process where Ni is precipitated under high pressure and temperature to obtain a "cauliflower" shaped particle [45]. The Al-powders manufactured by atomization show irregular shaped particles and sizes of 235 μm on average. The Y powder shows a combination of fine particles and agglomerates of irregular shape. The correspondent analysis of particle size distribution from those powders is shown in Figure 1d. From this plot, a wide range in the particle size distribution for Y and Al is observed, whereas Ni presented a uniform range of distribution. The size distribution of each powder is shown in Table 2.

The XRD patterns of the raw materials are shown in Figure 2. The phase identification was performed using JCPDF's 04-0850, 04-0787, and 33-1458 for Ni, Al, and Y, respectively. According to the patterns for Ni and Al powders, no secondary phases are present. The case of Y-powder presents partial oxidation, which is unavoidable at the measurement moment due to the high reactivity of the element at atmospheric conditions, and the oxide was identified using JCPDF 43-0661.

XRD results were fitted with the reference patterns using Rietveld refinement to obtain lattice parameters (Table 2). The obtained experimental values agree with the corresponding theoretical values (Table 2).

3.2 Characterization of the SHS conditions of the NiAl synthesis

As mentioned before, the SHS process was activated during specific milling conditions, which has been reported to obtain NiAl intermetallics [5–8].

Figure 3 shows the typical results of the NiAl intermetallic synthesis during the mechano-activation process. Figure 3a shows a representative curve of temperature vs. time depicting the conditions at which the SHS reaction takes place, identifying in different stages the reaction and maximal temperatures (T_{reac} and T_{max}, respectively) as well as the reaction time (t_{reac}). In the first stage, a continuous parabolic increase in temperature is observed, which corresponds to powder milling, particle deformation, flattening, fracturing, and cold welding. The second step is identified with a sharp increase in temperature that describes the exothermal reaction produced inside the vial during the SHS process, in which the B2 phase is formed. Finally, in the third stage, the temperature decreases as the milling process evolves, which purely describes the regime of size diminution of the NiAl alloy particles.

For a stoichiometric NiAl, a sharp peak is formed, evidencing the point for ignition of the self-propagating process, which is typically shown around 60 min. The reproducibility of the SHS process of pure NiAl after at least 5 milling tests showed $t_{reac} = 61 \pm 2$ min and $T_{reac} = 44 \pm 1.5$ ^{o}C. For a stoichiometric undoped NiAl alloy, the average values of lattice and order parameters are 2.8875 ± 0.0013 Å and 0.878, respectively.

Figure 3b shows the results of SHS reaction time vs. the total volume (milling media + powder volume) for three different BPR. From this graph, one can see that increasing the BPR, the SHS reaction time reduces and that for constant BPR, the reaction time shows a tendency to a linear increase as a function of total volume in the vial with different slopes as a function of the number of balls. Additionally, for high powder volume, the exothermal reaction does not occur, and the powder mixture tends to agglomerate during milling. The operation window identified in Fig. 3b shows the variation of parameters in which the NiAl phase occurs. As a result of the optimization of B2-NiAl synthesis by mechanical alloying, the optimal process variables to guarantee the synthesis of the NiAl phase were identified to be BPR 6: 1 and 3 balls. These parameters were selected for the synthesis of the B2-NiAlxY alloy.

On the other hand, for the conditions that need long milling times to activate the SHS reaction, a regime of contamination due to vial wear is present. These results are directly related to the net volume of powder inside the vial so that for higher powder volumes (V_4 = 1.7 cm^3 of powder), more energy or time is necessary to reach the synthesis conditions. A similar effect has been previously reported elsewhere [9].

NiAl powder synthesized by SHS belongs to the group of mechanochemically prepared materials or reactive materials in which the thermodynamically convenient stoichiometric composition of NiAl provides the conditions to achieve the heat of reaction for the synthesis of highly ordered intermetallic [6,7]. It is well known that Ni and Al belong to the combination of ductile-ductile metals, which are first cold–welded during milling, work-hardened and fragmented due to induced brittleness. It has also been demonstrated by TEM analysis that the NiAl synthesis mechanism during milling is diffusion controlled so that before the formation of B2-NiAl, additional phases, such as $NiAl_3$, Ni_2Al_3 are formed as the deformation energy is stored before the ignition reaction of NiAl takes place [46].

The effect of milling conditions on the long-range ordering and lattice parameters for pure NiAl are shown in Table 3. The results of the *S* parameter (also included in Figure 3b for each milling) tend to increase with the BPR and number of balls. On the other hand, the lattice parameter showed the closest values to the NiAl nominal parameter (2.887 Å) when milling with 3 balls [1]. From these data, the parameters to prepare the compositions containing Y were fixed to 3 balls and 5.3 g (V_3 of powder) of Ni-Al (powder (BPR 6:1) since it delivers the best combination of S and lattice parameter in terms of avoiding microstrains in the milled powder.

Under the selected conditions, the set of samples described in Table 1 was prepared by ball milling and subsequently pressed and densified by spark plasma sintering, allowing to keep the original phase leading to high densification.

3.3 Structural characterization of NiAl-Y alloys

The structural characterization of the milled powders and sintered alloys with different Y-content is shown in Figure 4. Figure 4a shows the XRD patterns of the sintered samples with different Y-content in the NiAl matrix. The B2-NiAl phase was identified using the JCPDF 44-1188. Rietveld refinement was performed to the XRD profiles for data analysis. The evolution of lattice parameters for both powder samples and sintered buttons as a function of the Y-content is shown in Figure 4b. The lattice constant of the B2-NiAl phase increases as a function of the Y content up to 0.7 at.% and remains stable for 1.0 and 1.5 at.%. This behavior is associated with the inclusion of Y in the B2-NiAl crystal structure of the samples sintered by SPS. In addition, the XRD patterns of samples containing 1.0 and 1.5 at.% Y show peaks associated with Y_2O_3, which is probably related to the solubility limit of Y in the NiAl alloy.

The experimental values obtained for the milled powders oscillate close to the B2-NiAl nominal value (2.8875 Å). A closer view of the evolution tendency in as-milled powders shows first, a decrease in the lattice parameter below the nominal value, and then, an increase at higher Y-content reaching the B2-NiAl nominal value. This behavior can be attributed to a combination of micro-lattice deformation and the partial incorporation of yttrium in a solid solution that balances this effect. On the other hand, a clear trend for sintered buttons can be observed, which shows first an increase of the lattice parameter up to a value of approx. 2.8910 Å, which is above the B2-NiAl nominal value. Based on these results, the solubility limit of Y in the NiAl unit cell of these alloys prepared by SHS+SPS seems to correspond to 0.5 at.% of yttrium. This value is higher than those reported elsewhere for bulk alloys [36].

A summary of these results that also include data of long ordering factor is given in Table 4. The B2-NiAl alloy obtained after the ball milling optimization process is highly ordered (S = 0.96). As can be seen from Table 4, the addition of Y decreases ordering to an average of 0.82 for doped NiAl alloys. This behavior is associated with the site preference of Y in the B2-NiAl structure and its effect on the relative intensity of the (100) superlattice peak. Reports of theoretical calculations have shown that Y and other transition metals have a remarked preference for Al sites in the B2-NiAl structure [47–49]. When Y takes the Al place, the B2-YNi interaction constitutes a minor difference in atomic scattering factors (DASF = 11) compared to that of the undoped system B2-NiAl (DASF = 15). Considering that DASF influences the intensity of the superlattice peaks in these types of crystal structures [50], the observed decrease in S in doped alloys is attributable to the inclusion of Y in the B2-NiAl structure.

Finally, figure 4c shows a typical SEM/EBSD micrograph of the undoped NiAl alloy after SPS. The EBSD image recorded with a step size of 50 nm was selected since it shows microstructural details of the NiAl sample taking advantage of the crystal orientation contrast. A non-texturized, dense microstructure of equiaxially shaped grains with a homogeneous grain size of 4.6 μm in average was obtained as a result of the SPS densification step.

3.4 Oxidation behavior by TGA

As mentioned before, the effect of Y content on the oxidation behavior at 1100 ^{o}C of sintered NiAl samples was evaluated by measuring the weight gain by thermogravimetric analysis done for 10 h in an air atmosphere of representative sintered buttons (0.0, 0.3, 0.5, 1, and 1.5at. %). No top-coat has been considered in these samples. The corresponding results are shown in Figure 5. Having the behavior of undoped NiAl as a reference, where a rapid mass increase followed by a substantial flattening of the curve is noticed, a clear effect of the Y-content in bare NiAl buttons is observed. The weight gain is reduced for samples with lower Y content such as 0.3 and 0.5 at.%. The trend of a higher oxidation rate with higher Y-content is remarkably clear in the current data. Surprisingly, the initial oxide growth rate is lower for all Y-doped NiAl versions having contents up to 1.0 at.% in comparison to pure NiAl. A parabolic rate constant of 1.02×10^{-5} mg^{2} cm^{-4} s^{-1} was observed for NiAl, which is smaller compared with data reported by Poquillon [51] whose results are included in a range of 2.2×10^{-6} to 8×10^{-7} mg^{2} cm^{-4} s^{-1}. The instantaneous parabolic rate constant for each composition was calculated using the local fitting procedure proposed by Monceau and Pieraggi [52] for the general parabolic law:

$$t = A + B\Delta m + C\Delta m^2 \qquad \text{(Eq 2)}$$

Where *A* and *B* are coefficients related to different kinetic parameters, and *C* is inversely proportional to the k_p value.

Considering the rest of the TGA curves, in the 0.3 at.% Y sample the oxidation kinetics was reduced. In this particular case, the parabolic rate constant value is higher compared to values previously reported elsewhere [37].

Figure 6a shows that for the time dependence of k_p for the oxidized during isothermal oxidation as a function of Y-content, a steady-state regime is reached at around 4 h of treatment. The calculated k_p values after 10 h are plotted on the Arrhenius plot in Figure 6b, showing the effect of Y-content on the k_p values of NiAl sintered samples. Bold lines refer to Brumm and Grabke data for a single crystal NiAl [53]. The undoped NiAl alloy and the NiAl_1.0Y and NiAl_1.5Y samples present k_p values higher in one order of magnitude compared to the 0.3, 0.5 at.% Y-doped alloys. These results are also reflected in the predominance of the oxide phases, where the compositions NiAl_0.3Y and NiAl_0.5Y are found in the transition from θ-Al_2O_3 to α-Al_2O_3, which suggests that at longer times of exposure, the formation of α-Al_2O_3 can be completed. However, a clear tendency to form α-Al_2O_3 is observed, whereas compositions higher than 1 at.% Y exhibit a predominance of θ-Al_2O_3 phase. The beneficial effect of Y on NiAl oxidation behavior has been demonstrated at this point.

3.5 Furnace cyclic tests

The measured mass gain after furnace cyclic tests at 1100 ^{o}C of 7YSZ coated buttons of samples in an extended composition range (0.1, 0.3, 0.5, 0.7, 1, and 1.5 at.% Y) are shown in Figures 7 and 8. As mentioned before, these samples were tested after one side 7YSZ deposition by EB-PVD. During the deposition process, which is carried out in an oxidizing atmosphere, the formation of a thermally grown oxide is expected on both sides of the samples, the TBC coated and the bare intermetallic side. In the current model system, diffusion is purely outward leading to an oxide scale, and a single interface is formed opposite to the multiple interfaces expected from an overlay coated superalloy system. Thus, differences in time to failure can be directly associated with the influence of the Y-content. The oxidation behavior for the first 100 cycles in FCT as a function of Y-content is shown in Figure 7a. In most cases, a steady state in weight gain can be observed till 100 cycles. The state of each sample after 100 cycles in FCT, where the complete top coat is still attached to the alloy, is shown in Figure 7b, except for the NiAl sample where a clear loss of weight after the 25th cycle was observed.

Long term cycles to failure of the TBC systems in furnace cyclic tests at 1100 °C are shown in Figure 8. Some samples were removed early either for further analysis (0.5 at.%) or failure reasons (0.1 at.%). From this plot, low Y-content samples (0.1-0.5 at.%) continued showing the lowest weight gain over hundreds of cycles. However, the only samples that hold for the total range of 2000 cycles are those doped with 1 and 1.5 at.% Y even when they showed the highest oxidation kinetics. Thus, it can be seen that the low oxidation behavior and lifetime are not always coupled, i.e., the samples having the highest Y-level did show the highest weight gain but provided the best adhesion of TGO and TBC. Based on these results, it is clear that Y is prompt to diffuse outward first to the surface due to the potential oxygen gradient creating nucleation sites that help to the formation of a dense TGO. It is well known that this process inhibits the outward diffusion of Al^{3+} cations by reducing chemical activity. As a result, the α-Al_2O_3 scale grew with a low kinetic constant predominantly by inward transport of O^{2-} anions, mainly along the scale grain boundaries.

Irrespective of the type of exposure at 1100 ºC, the protective effect of Y-additions is present even with contents as high as 1.5 at.% from both experimental approaches. For instance, either for 10 h in TGA or FCT the mass gain of the 1.5 at.% Y sample reaches similar values respective to the undoped NiAl. From these data, one can conclude that contents lower than 0.5 at.% show clear benefits in the first stages of oxidation behavior.

In a comparison between TGA and FCT results, for the first 10 cycles of FCT at 1100 ºC, the results of the mass gain are lower than the correspondent obtained with TGA (three times lower, always below 0.4 mg/cm^2). This behavior is again not surprising since after EB-PVD deposition the system already comprises a well-developed oxidation scale. For longer cycles, the general effect of net mass gain after FCT reveals the same tendency as for the TGA results. Consistently, the lowest mass gain is observed for the 0.1 and similar to the 0.3 at.% Y sample (regardless of fewer experimental points) showing a parabolic rate constant of 1.68E-7 $mg/cm^4\ s^{-1}$.

A summary of the results of the first stages of oxidation kinetics in terms of the parabolic rate constants obtained from TGA and FCT measurements is included in Table 5. In both cases that the k_p value increases as the Y content increases and the k_p for the 1 and 1.5 at.% are one order of magnitude higher than the remaining compositions with lower Y contents. Furthermore, samples oxidized by FCT presented lower k_p values than the samples exposed on TGA.

The microstructure of the TGO was analyzed after 100 cycles in FCT in the 0.5 at.% Y sample, which showed low oxidation kinetics. The correspondent SEM micrographs on the cross-section are shown in Figure 9. The top coat presents the typical columnar morphology. A TGO has formed on top of the NiAl-0.5Y button similarly as observed in bond coated superalloy TBC systems. The upper part of the oxide layer consists of a mixed zone showing finely dispersed zirconia particles within alumina, which is attributed to phase transformations and diffusion processes [54]. Further on, a YAG phase was detected both on the middle and bottom of the TGO layer, probably due to the reaction of the alumina with some oxidized particles of Y.

Traces of finely dispersed yttrium oxide particles were identified in the micrographs of the as-sintered samples (micrographs not shown here). This issue is expected to be systematically observed in the different compositions, without affecting the reactive element effect in the oxidation tests.

Based on these results, the improvement in the scale adhesion due to small Y additions to NiAl alloy confirmed previously known effects, such as oxidation rate reduction, increase the Al_2O_3 scale adherence [38–40], and modification of its microstructural characteristics leading to sites for heterogeneous nucleation of the TGO, avoiding the growth of metastable oxides [41]. As a result, Y increased the adhesion properties on the NiAl/TGO/TC interfaces and thus the number of cycles to failure of the TBC system [38,40,42]. Finally, evidence has been presented showing that the solubility limit of Y in these NiAl alloys is below 0.5 at.%, which matches data reported elsewhere [36].

4. Conclusions

- NiAl buttons sintered by SPS from highly ordered intermetallic powder synthesized by self-propagating high-temperature synthesis (SHS) have shown to be a great model system to effectively evaluate the effect of yttrium as a reactive element to enhance the oxidation protection behavior of Ni-based bond coats and to evaluate the effect of yttrium concentration on the life time of thermal barrier coatings.
- Highly reproducible SHS of NiAl-Y was successfully activated in a SPEX 8000D mixer mill. The powders contained between 0 and 1.5 at.% Y and were sintered in dense coupons by spark plasma sintering.

- A clear effect of Y additions was observed in the crystalline structure of the alloy, considering the increase of the lattice parameters coupled with the Y content as well as their mass gain on the oxidation experiments. Low Y contents reduce the oxidation growth kinetics as measured by TGA and in furnace cyclic tests considerably leading for the 0.1 to 0.5 at.% Y samples to roughly only one third of the mass gain of the un-doped NiAl.
- The longest TBC lives and lowest spallation rates of an 7YSZ EB-PVD TBC deposited on the NiAl containing various Y concentrations were achieved for samples having higher Y contents such as 1.0 and 1.5 at.%, although those showed the highest mass gains.
- Overall, nearly all Y-doped samples improved both, oxidation behavior and TBC live in comparison to pure NiAl.

Acknowledgments

J.M.S. thanks CONACyT and the Alexander von Humboldt Foundation for financial support for research activities at the German Aerospace Center (DLR). Authors thank J. Duarte and A. Kostka for support in SEM/EBSD measurements. This work has been partially supported by CONACyT and carried out at CENAPROT and LIDTRA national laboratories.

References

[1] D.B. Miracle, the Physical a N D Mechanical Properties of NiAl, Acta Mater. 41 (1993) 649–684.

[2] F. Scheppe, P.R. Sahm, W. Hermann, U. Paul, J. Preuhs, Nickel aluminides: A step toward industrial application, Mater. Sci. Eng. A. 329–331 (2002) 596–601. https://doi.org/10.1016/S0921-5093(01)01587-8.

[3] G. Frommeyer, R. Rablbauer, High temperature materials based on the intermetallic compound NiAl reinforced by refractory metals for advanced energy conversion technologies, Mater. Sci. Eng. A. 3 (2008) 1–7. https://doi.org/10.2374/SRI08SP101-79-2008-507.

[4] S. Wu, X. Wu, R. Wang, Q. Liu, L. Gan, Effects of Ni vacancy, Ni antisite, Cr and

Pt on the third-order elastic constants and mechanical properties of NiAl, Intermetallics. 55 (2014) 108–117. https://doi.org/10.1016/j.intermet.2014.04.022.

[5] M. Atzmon, Characterization of AlNi formed by a self-sustaining reaction during mechanical alloying, Mater. Sci. Eng. A. 134 (1991) 1326–1329. https://doi.org/10.1016/0921-5093(91)90983-T.

[6] J. Subrahmanyam, M. Vijayakumar, Self-propagating high-temperature synthesis, J. Mater. Sci. 27 (1992) 6249–6273. https://doi.org/10.1007/BF00576271.

[7] L. Takacs, Self-sustaining reactions induced by ball milling: An overview, Int. J. Self-Propagating High-Temperature Synth. 18 (2009) 276–282. https://doi.org/10.3103/s1061386209040086.

[8] E.T. Kubaski, O.M. Cintho, J.D.T. Capocchi, Effect of milling variables on the synthesis of NiAl intermetallic compound by mechanical alloying, Powder Technol. 214 (2011) 77–82. https://doi.org/10.1016/j.powtec.2011.07.038.

[9] C. Suryanarayana, Mechanical alloying and milling suryanaraya, Mater. Sci. 46 (2001) 1–184.

[10] C. Suryanarayana, Recent developments in mechanical alloying, Rev. Adv. Mater. Sci. 18 (2008) 203–211.

[11] M. Tokita, Spark Plasma Sintering (SPS) Method, Systems, and Applications, in: Handb. Adv. Ceram. Mater. Appl. Process. Prop. Second Ed., 2013: pp. 1149–1177. https://doi.org/10.1016/B978-0-12-385469-8.00060-5.

[12] M. Tokita, Mechanism of Spark Plasma Sintering, in: Proc. Int. Symp. Microwave, Plasma Thermochem. Process. Adv. Mater., 1997: pp. 67–76. https://doi.org/10.1063/1.3622584.

[13] A. Michalcová, D. Vojtech, T.F. Kubatík, P. Novák, P. Dvorak, P. Svobodová, I. Marek, NiAl intermetallic prepared with reactive sintering and subsequent powder-metallurgical plasma-sintering compaction, Mater. Tehnol. 50 (2016) 447–450. https://doi.org/10.17222/mit.2015.089.

[14] D. Li, H. Guo, D. Wang, T. Zhang, S. Gong, H. Xu, Cyclic oxidation of β-NiAl with

various reactive element dopants at 1200°C, Corros. Sci. 66 (2013) 125–135. https://doi.org/10.1016/j.corsci.2012.09.010.

[15] D. Wang, H. Peng, S. Gong, H. Guo, NiAlHf/Ru: Promising bond coat materials in thermal barrier coatings for advanced single crystal superalloys, Corros. Sci. 78 (2014) 304–312. https://doi.org/10.1016/j.corsci.2013.10.013.

[16] D.P. Moon, Role of reactive elements in alloy protection, Mater. Sci. Technol. 5 (1989) 754–764. https://doi.org/10.1179/mst.1989.5.8.754.

[17] B.A. Pint, Experimental Observations in Support of the Dynamic-Segregation Theory to Explain the Reactive-Element Effect, Oxid. Met. 45 (1996) 1–37.

[18] S. Hou, S. Zhu, T. Zhang, F. Wang, A magnetron sputtered microcrystalline β-NiAl coating for SC superalloys. Part I. Characterization and comparison of isothermal oxidation behavior at 1100 °c with a NiCrAlY coating, Appl. Surf. Sci. 324 (2015) 1–12. https://doi.org/10.1016/j.apsusc.2014.10.106.

[19] M. Schumann, E. Yang, J.C. Graham, M.J. Ruhle, The effect of Y and Zr on the oxidation of NiAl, Mater. Corros. 47 (1996) 631–632.

[20] B. Ning, M. Shamsuzzoha, M.L. Weaver, Influence of processing variables on the properties of dc magnetron sputtered NiAl coatings containing Hf additions, J. Vac. Sci. Technol. A Vacuum, Surfaces, Film. 23 (2005) 44. https://doi.org/10.1116/1.1828085.

[21] B.A. Pint, Progress in Understanding the Reactive Element Effect Since the Whittle and Stringer Literature Review, in: P.F. Tortorelli, I.G. Wright, P.Y. Hou (Eds.), John Stringer Symp. High Temp. Corros., ASM International, 2003: pp. 9–19.

[22] B. Hazel, J. Rigney, M. Gorman, B. Boutwell, R. Darolia, Development of improved bond coat for enhanced turbine durability, in: Proc. Int. Symp. Superalloys, 2008: pp. 753–760.

[23] M.A. Bestor, R.L. Martens, R. a. Holler, M.L. Weaver, Influences of annealing and hafnium concentration on the microstructures of sputter deposited B-NiAl coatings on superalloy substrates, Intermetallics. 18 (2010) 2159–2168. https://doi.org/10.1016/j.intermet.2010.07.001.

[24] M.A. Bestor, J.P. Alfano, M.L. Weaver, Influences of chromium and hafnium additions on the microstructures of β-nial coatings on superalloy substrates, Intermetallics. 19 (2011) 1693–1704. https://doi.org/10.1016/j.intermet.2011.06.020.

[25] S. Hamadi, M.P. Bacos, M. Poulain, A. Seyeux, V. Maurice, P. Marcus, Oxidation resistance of a Zr-doped NiAl coating thermochemically deposited on a nickel-based superalloy, Surf. Coatings Technol. 204 (2009) 756–760. https://doi.org/10.1016/j.surfcoat.2009.09.073.

[26] R. Darolia, NiAl alloys for high-temperature structural applications, JOM. 43 (1991) 44–49. https://doi.org/10.1007/BF03220163.

[27] A.I. Kovalev, R.A. Barskaya, D.L. Wainstein, Effect of alloying on electronic structure, strength and ductility characteristics of nickel aluminide, in: Surf. Sci., 2003: pp. 35–40. https://doi.org/10.1016/S0039-6028(03)00208-5.

[28] A. Strawbridge, P.Y. Hou, The role of reactive elements in oxide scale adhesion, Mater. High Temp. 12 (1994) 177–181. https://doi.org/10.1080/09603409.1994.11689484.

[29] A. Strawbridge, R.A. Rapp, The Role of Reactive Elements on Scale Growth in High-Temperature Oxidation of Pure Nickel, Iron, Cobalt, and Copper, J. Electrochem. Soc. 141 (1994) 1905. https://doi.org/10.1149/1.2055025.

[30] B.A. Pint, Optimization of Reactive-Element Additions to Improve Oxidation Performance of Alumina-Forming Alloys, J. Am. Ceram. Soc. 86 (2003) 686–95. https://doi.org/10.1111/j.1151-2916.2003.tb03358.x.

[31] D. Naumenko, B.A. Pint, W.J. Quadakkers, Current Thoughts on Reactive Element Effects in Alumina-Forming Systems: In Memory of John Stringer, Oxid. Met. 86 (2016) 1–43. https://doi.org/10.1007/s11085-016-9625-0.

[32] A.U. Munawar, U. Schulz, M. Shahid, Microstructure and lifetime of EB-PVD TBCs with Hf-doped bond coat and Gd-zirconate ceramic top coat on CMSX-4 substrates, Surf. Coatings Technol. 299 (2016) 104–112. https://doi.org/10.1016/j.surfcoat.2016.05.005.

[33] B.A. Pint, K.L. More, I.G. Wright, Effect of quaternary additions on the oxidation

behavior of Hf-doped NiAl, Oxid. Met. 59 (2003) 257–283. https://doi.org/10.1023/A:1023087926788.

[34] B.A. Pint, The role of chemical composition on the oxidation performance of aluminide coatings, Surf. Coatings Technol. 188–189 (2004) 71–78. https://doi.org/10.1016/j.surfcoat.2004.08.007.

[35] A. Ebach-Stahl, U. Schulz, R. Swadźba, A.U. Munawar, Lifetime improvement of EB-PVD 7YSZ TBCs by doping of Hf or Zr in NiCoCrAlY bond coats, Corros. Sci. 181 (2021). https://doi.org/10.1016/j.corsci.2020.109205.

[36] V. Raghavan, Al-Ni-Y (Aluminum-Nickel-Yttrium), J. Phase Equilibria Diffus. 31 (2010) 57–58. https://doi.org/10.1007/s11669-009-9625-8.

[37] W. Chen, X. Shan, Y. Guo, J. Li, Z. Zou, F. Guo, X. Zhao, P. Xiao, The effect of reactive element species and concentrations on the isothermal oxidation of β-NiAl coating fabricated by spark plasma sintering, Surf. Coatings Technol. (2019). https://doi.org/10.1016/j.surfcoat.2018.10.071.

[38] J. Jedliński, S. Mrowec, The influence of implanted yttrium on the oxidation behaviour of β-NiAl, Mater. Sci. Eng. 87 (1987) 281–287. https://doi.org/10.1016/0025-5416(87)90390-9.

[39] J. Jedliński, J.L. Grosseau Poussard, G. Smoła, G. Bonnet, M. Nocuń, K. Kowalski, J. Dąbek, The effect of alloyed andyor implanted yttrium on the mechanism of the scale development on β-NiAl at 1100°C, Mater. High Temp. 29 (2012) 59–69. https://doi.org/10.3184/096034012X13349146318471.

[40] J.G. Smeggil, Some comments on the role of yttrium in protective oxide scale adherence, Mater. Sci. Eng. 87 (1987) 261–265. https://doi.org/10.1016/0025-5416(87)90387-9.

[41] J. Jedliński, Comments on the effect of yttrium on the early stages of oxidation of alumina formers, Oxid. Met. (1993). https://doi.org/10.1007/BF00666609.

[42] S. Bose, Thermal Barrier Coatings (TBCs), in: High Temp. Coatings, 2007: pp. 155–232. https://doi.org/DOI: 10.1016/B978-075068252-7/50008-1.

[43] W. Chen, L. He, Y. Guo, X. Shan, J. Li, F. Guo, X. Zhao, N. Ni, P. Xiao, Effects of reactive element oxides on the isothermal oxidation of β-NiAl coatings fabricated by spark plasma sintering, Surf. Coatings Technol. (2019). https://doi.org/10.1016/j.surfcoat.2018.10.021.

[44] H. Ruiz-Luna, J.M. Alvarado-Orozco, L.A. Cáceres-Díaz, I. López-Báez, J. Moreno-Palmerín, F.J. Espinoza-Beltrán, M.S. Boldrick, G. Trápaga-Martínez, J. Muñoz-Saldaña, Structural evolution of B2-NiAl synthesized by high-energy ball milling, J. Mater. Sci. 48 (2013) 265–272. https://doi.org/10.1007/s10853-012-6741-3.

[45] L. Koehler, K. Associates, Powder Metallurgy Nickel and Nickel Alloys, Powder Metall. 7 (2018) 673–681. https://doi.org/10.31399/asm.hb.v07.a0006122.

[46] G. Fan, L. Geng, Y. Feng, X. Cui, X. Yan, Solid State Reaction Mechanism and Microstructure Evolution of Ni-Al Powders during High Energy Ball Milling Revisited by TEM, Microsc. Microanal. 21 (2015) 953–960. https://doi.org/10.1017/S1431927615013501.

[47] H. Hu, S. Li, Y. Ren, W. Liu, H. Zhao, Site preference and brittle–ductile transition mechanism of B2-NiAl with ternary elements additions form first-principles calculations, Phys. B Condens. Matter. 576 (2020) 411703. https://doi.org/10.1016/j.physb.2019.411703.

[48] A. V. Ponomareva, E.I. Isaev, Y.K. Vekilov, I.A. Abrikosov, Site preference and effect of alloying on elastic properties of ternary B 2 NiAl-based alloys, Phys. Rev. B - Condens. Matter Mater. Phys. 85 (2012) 1–10. https://doi.org/10.1103/PhysRevB.85.144117.

[49] C. Jiang, Site preference of transition-metal elements in B2 NiAl: A comprehensive study, Acta Mater. 55 (2007) 4799–4806. https://doi.org/10.1016/j.actamat.2007.04.049.

[50] B.D. Cullity, S.R. Stock, Elements of X-Ray diffraction, Third edit, Pearson Education, 2014.

[51] D. Poquillon, D. Oquab, B. Viguier, F. Sénocq, D. Monceau, High-temperature oxidation kinetics of NiAl single crystal and oxide spallation as a function of

crystallographic orientation, Mater. Sci. Eng. A. 381 (2004) 237–248. https://doi.org/10.1016/j.msea.2004.04.009.

[52] D. Monceau, B. Pieraggi, Determination of Parabolic Rate Constants from a Local Analysis of Mass-Gain Curves, Oxid. Met. 50 (1998) 477–493. https://doi.org/10.1023/A:1018860909826.

[53] M.W. Brumm, H.J. Grabke, The Oxidation Behavior of NiAl-I. Phase Transformations on the Alumina Scale During Oxidation of NiAl and NiAl-Cr Alloys, Corros. Sci. 33 (1992) 1677–1690.

[54] A.G. Mora-García, H. Ruiz-Luna, J.M. Alvarado-Orozco, G.C. Mondragón-Rodríguez, U. Schulz, J. Muñoz-Saldaña, Microstructural analysis after furnace cyclic testing of pre-oxidized ReneN5/(Ni,Pt)Al/7YSZ thermal barrier coatings, Surf. Coatings Technol. 403 (2020) 126376. https://doi.org/10.1016/j.surfcoat.2020.126376.

Figures caption

Figure 1. SEM micrographs of the raw materials a) Ni, b) Al, c) Y-precursor. The particle size distribution of the samples is also shown (d).

Figure 2. XRD patterns of the raw materials.

Figure 3. Results of the NiAl intermetallic synthesis during the mechanoactivation process. a) Temperature evolution of Ni-Al powder mixtures during ball milling. A sharp peak evidencing the self-propagating process is shown around 60 minutes. b) Used process parameters showing the reaction time (min) vs volume of vial and their combined influence on the long-range ordering parameter. Limits of the synthesis process for either agglomeration or contamination due to vial use are also shown.

Figure 4. a) XRD patterns of the synthesized alloys and b) Evolution of lattice parameter of synthesized powder and sintered buttons as a function of yttrium content.

Figure 5. Weight gain during oxidation measurements of NiAl buttons in TGA and as a function of Y-content.

Figure 6. Analysis of oxidation behavior a) Log k_p plotted as a function of time for NiAl-Y samples during TGA isothermal oxidation as a function of Y content and b) Arrhenius plot showing the effect of Y-content on the k_p values of NiAl sintered samples. Bold lines refer to Brumm and Grabke data for a single crystal NiAl.

Figure 7. a) Weight gain during oxidation measurements of 7YSZ EB-PVD coated NiAl buttons after 100 cycles in FCT. b) State of the samples after 100 cycles in FCT.

Figure 8. Lifetime behavior of the tested samples up to 2000 cycles in FCT. The only samples that hold for the total range are those doped with 1 and 1.5 at.% Y.

Figure 9. Cross section of 7YSZ coated NiAl button doped with 0.5 at.% after 100 cycles showing the characteristics of TGO and the interfaces with 7YSZ top coat and the NiAl substrate.

Tables caption

Table 1. Composition in at.% of Y doped NiAl samples.

Table 2. Size distribution and structural characteristics of the starting powders.

Table 3. Summary of lattice and long-range parameters as a function of milling parameters of NiAl powders.

Table 4. Lattice parameters and long ordering factor of sintered NiAl-Y samples.

Table 5. Parabolic rate constants obtained for each alloy on TGA and FCT oxidation processes.

Figure 1

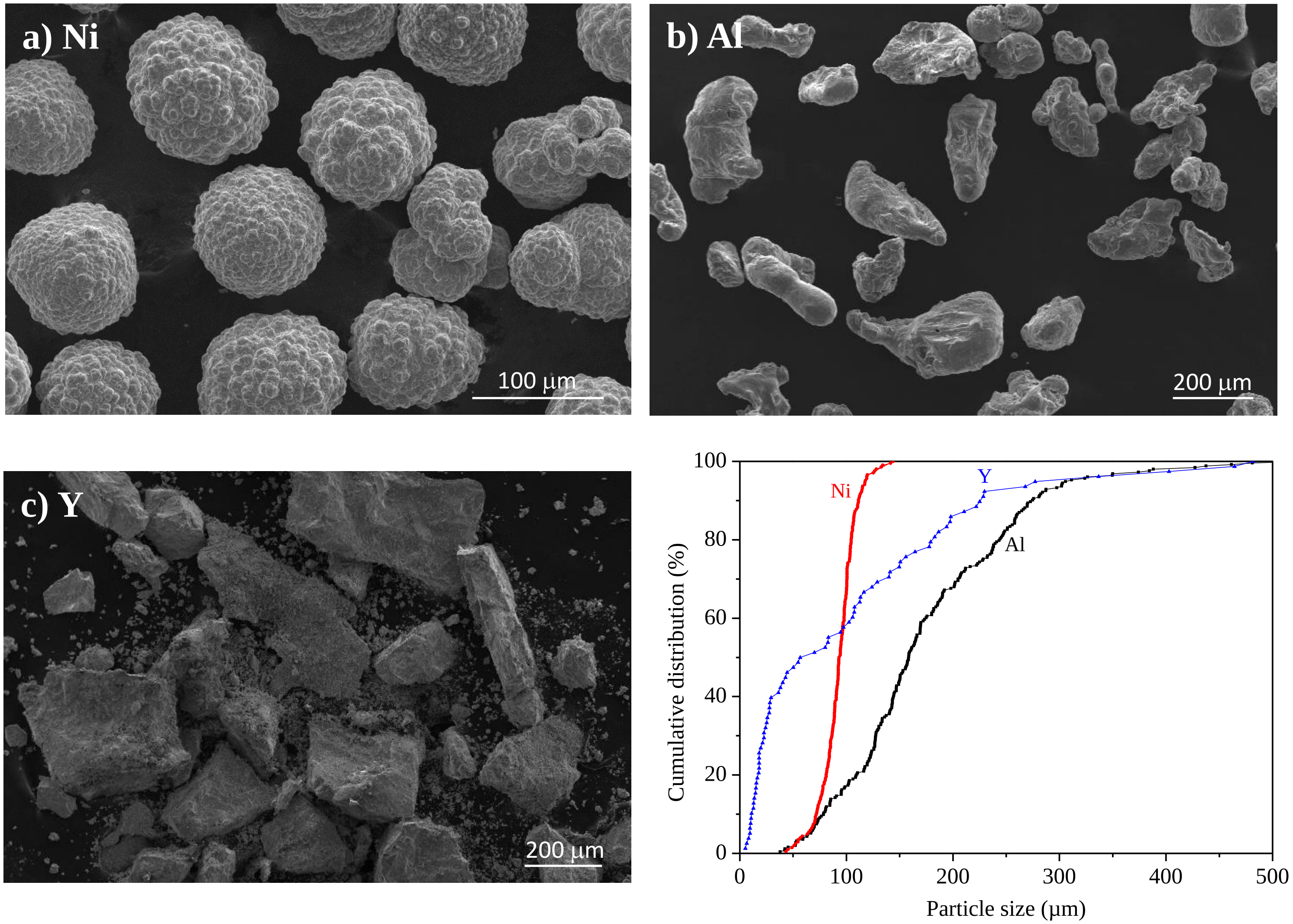

Muñoz Saldaña *et al.*

Figure 2

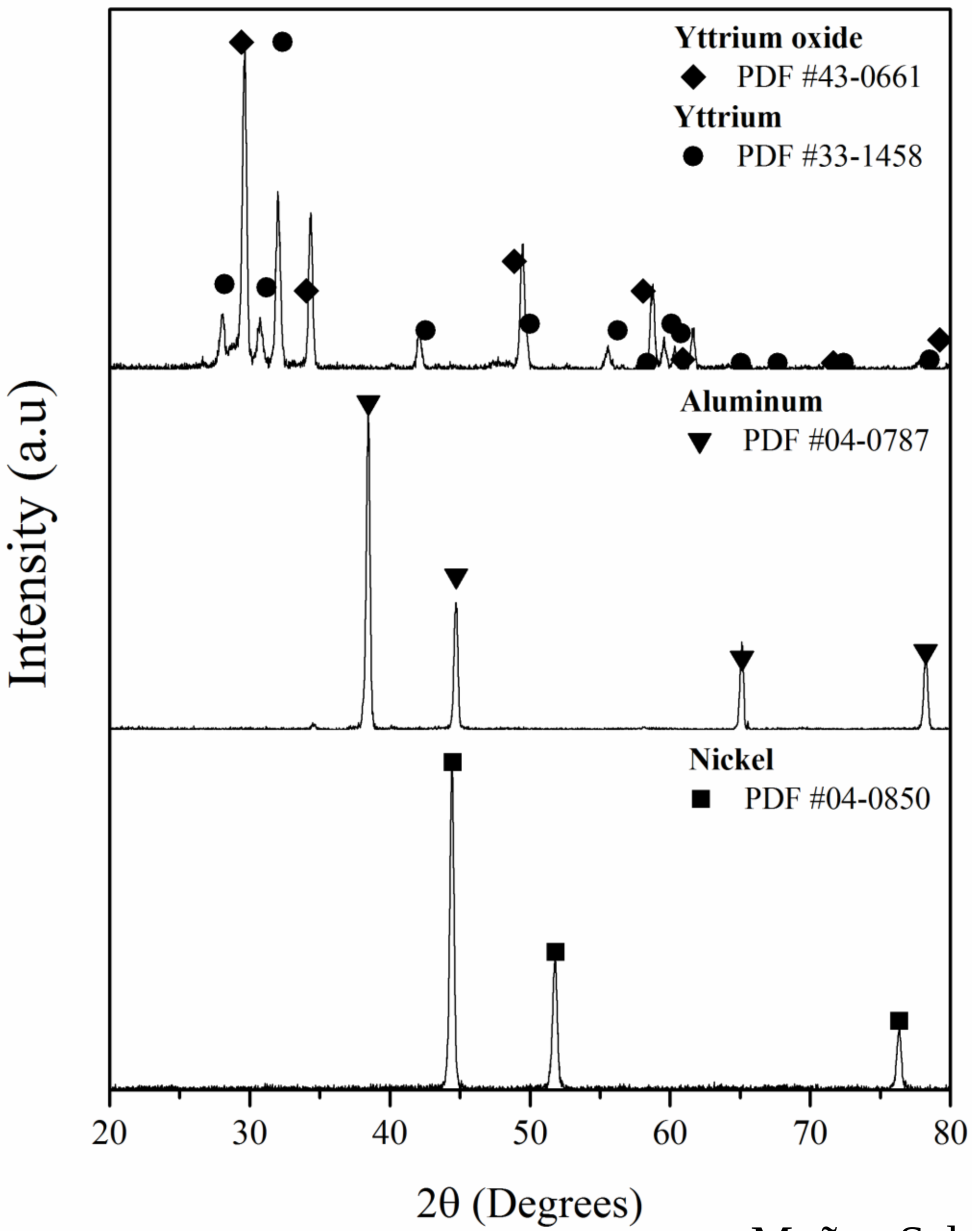

Muñoz Saldaña *et al.*

Figure 3

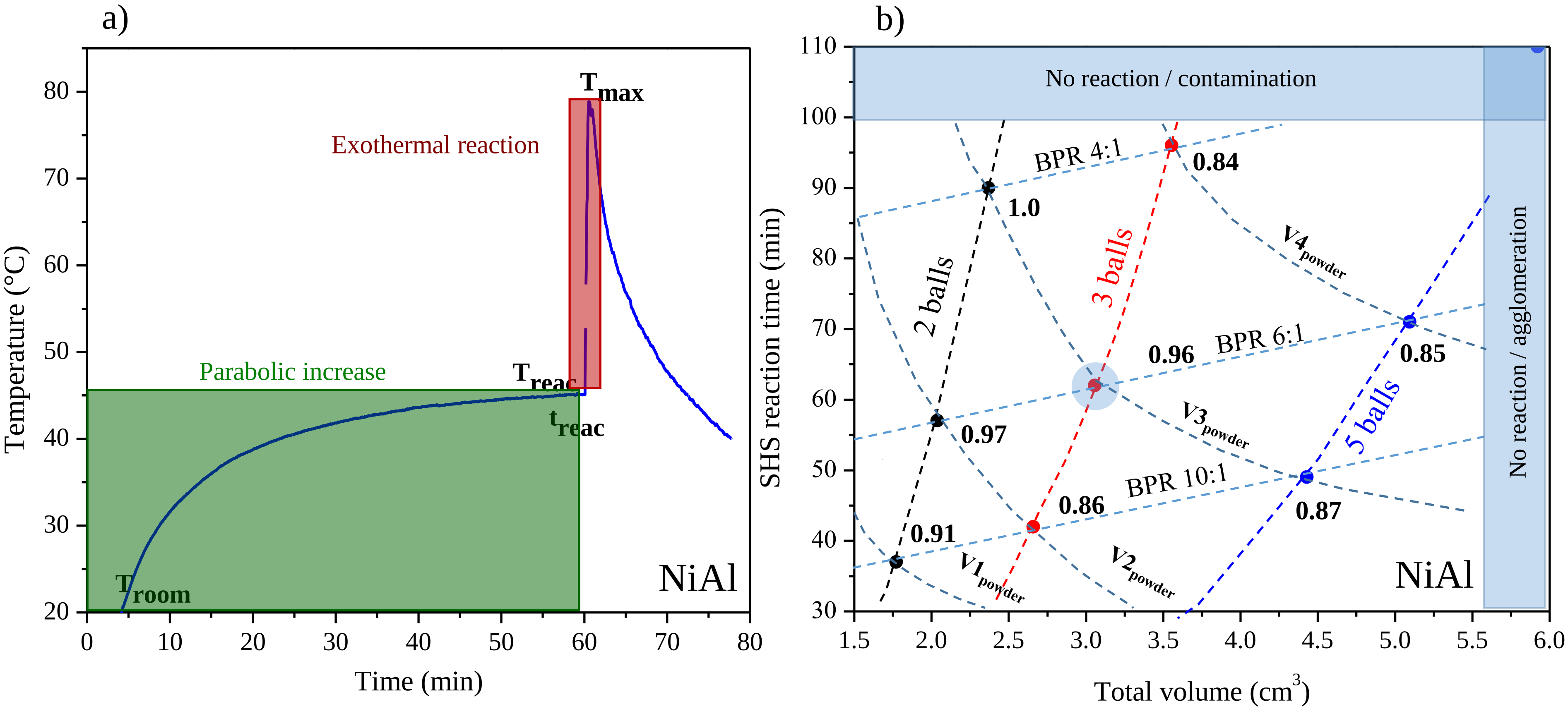

Muñoz Saldaña *et al.*

Figure 4

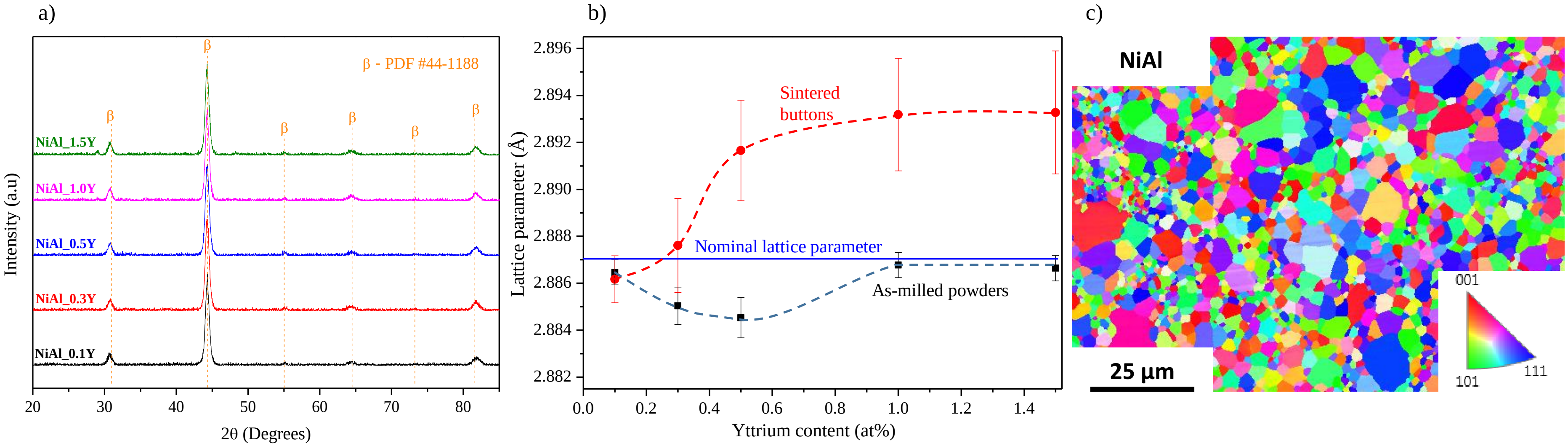

Muñoz Saldaña *et al.*

Figure 5

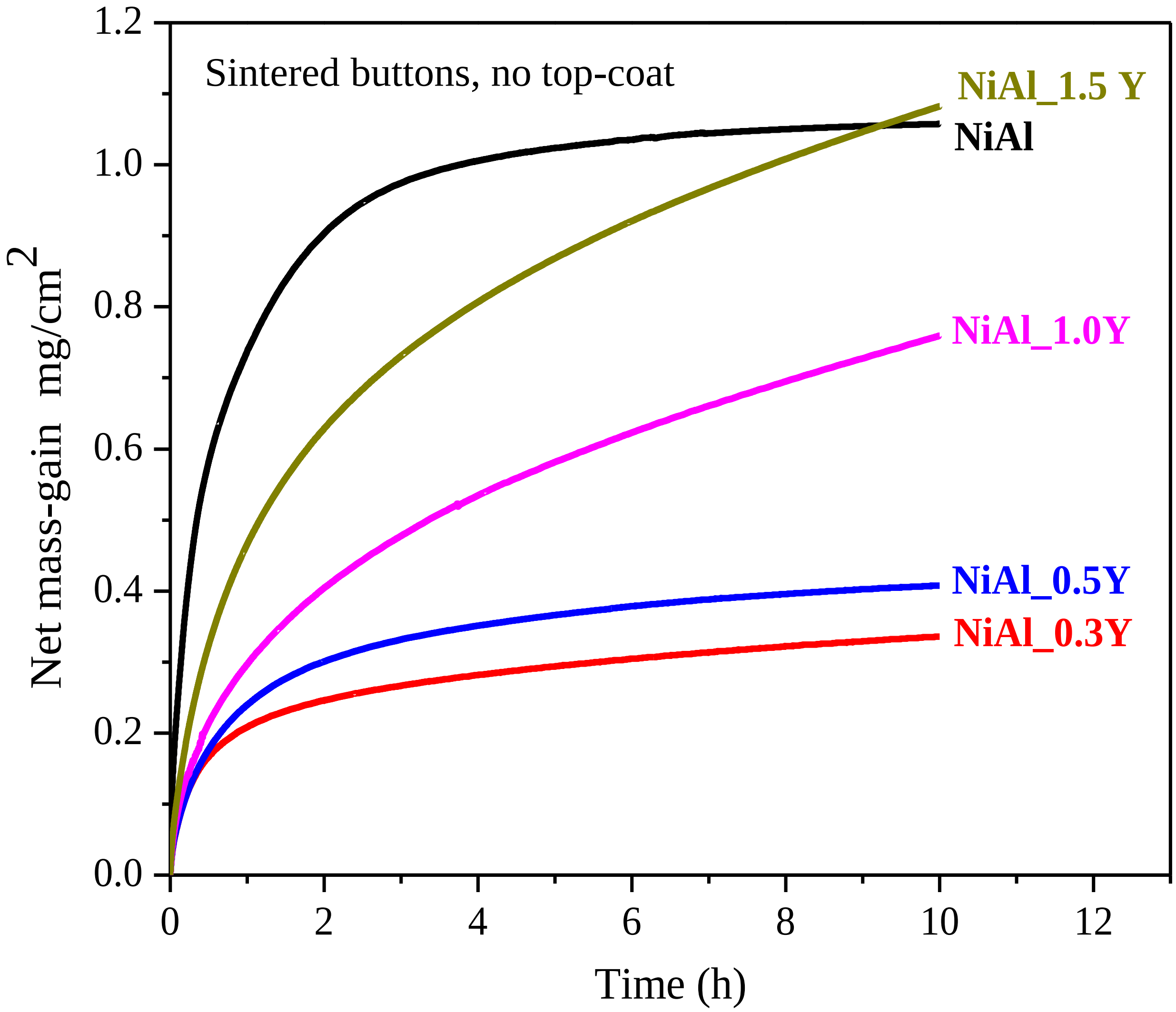

Muñoz Saldaña *et al.*

Figure 6

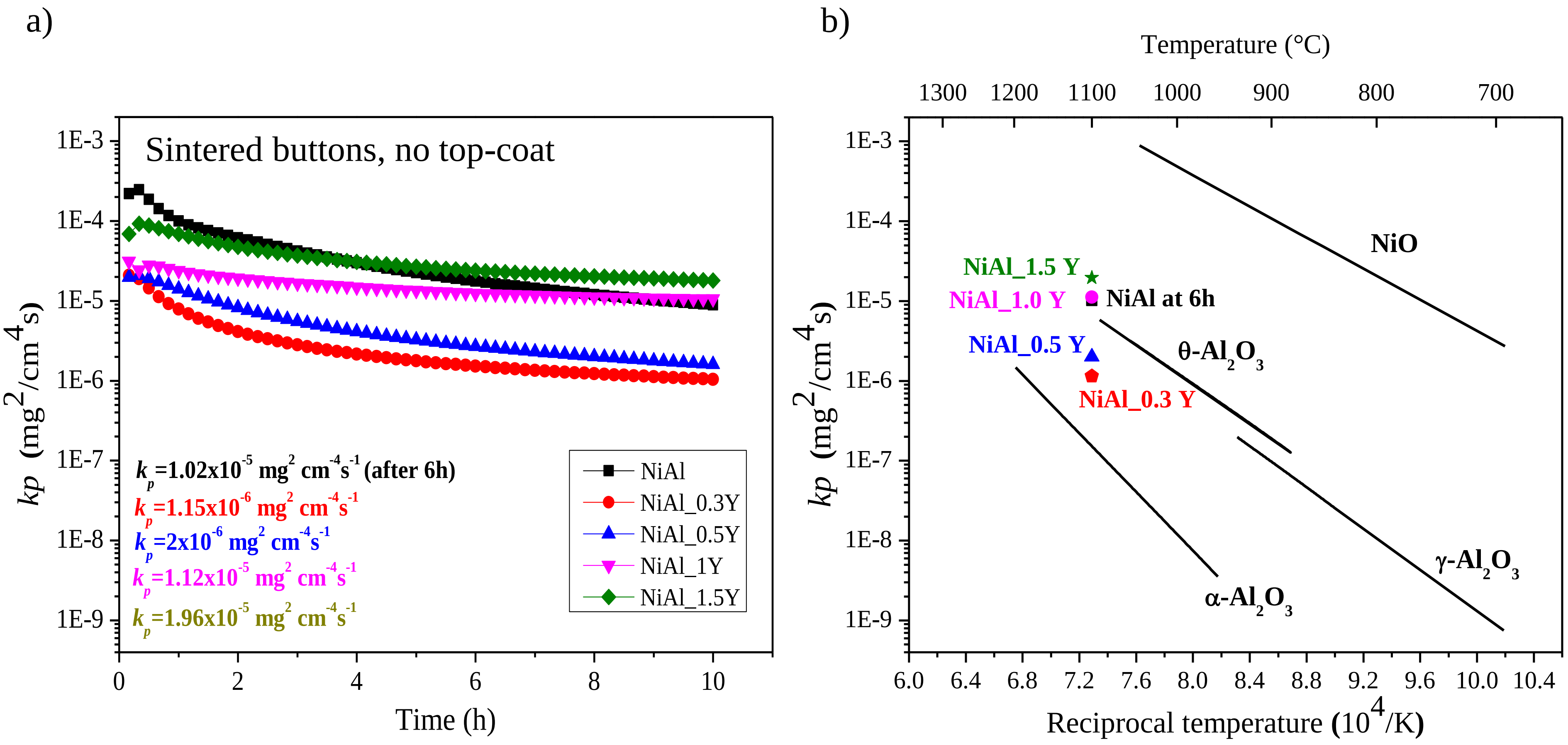

Muñoz Saldaña *et al.*

Figure 7

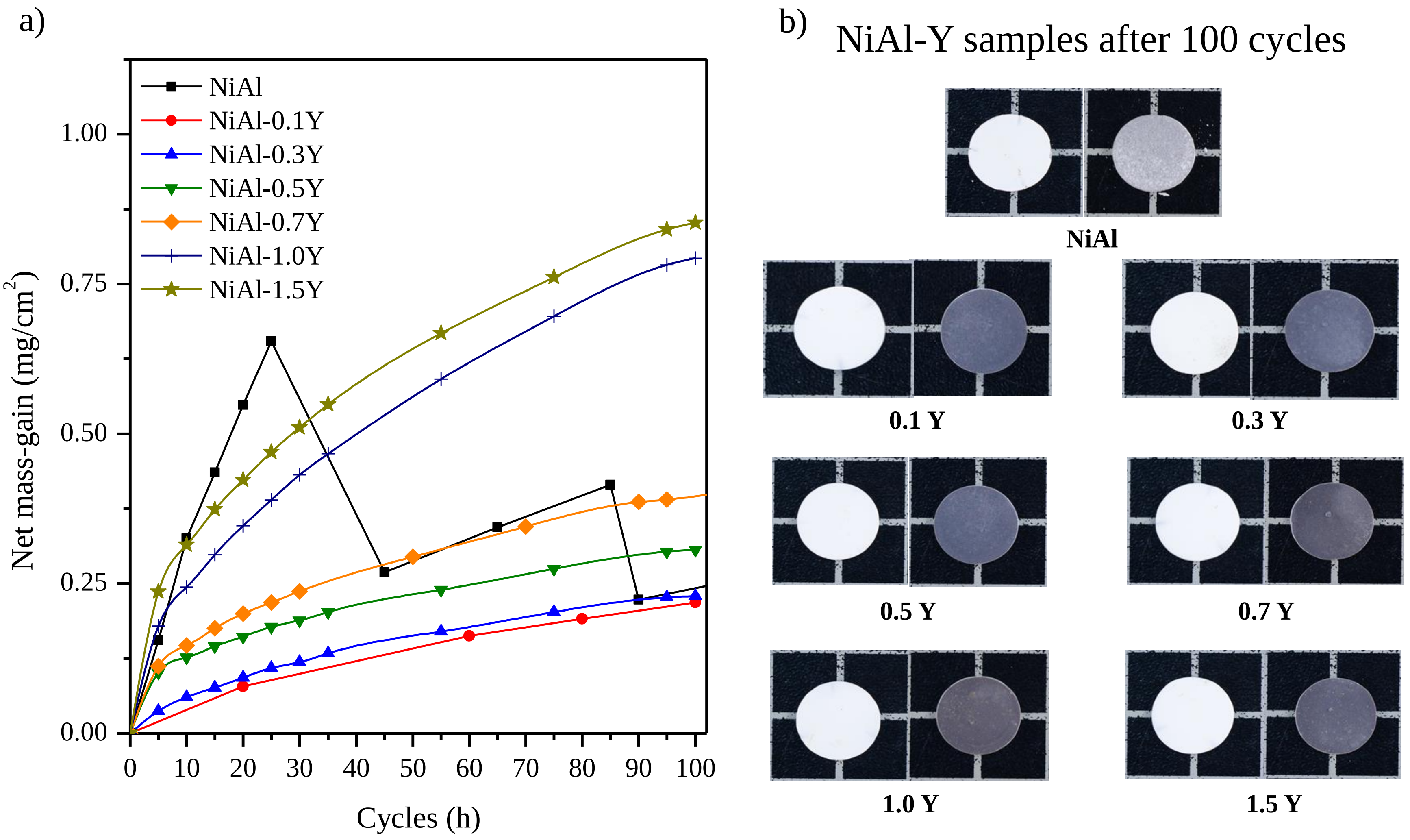

NiAl-Y samples after 100 cycles

NiAl

0.1 Y

0.3 Y

0.5 Y

0.7 Y

1.0 Y

1.5 Y

Muñoz Saldaña *et al.*

Figure 8

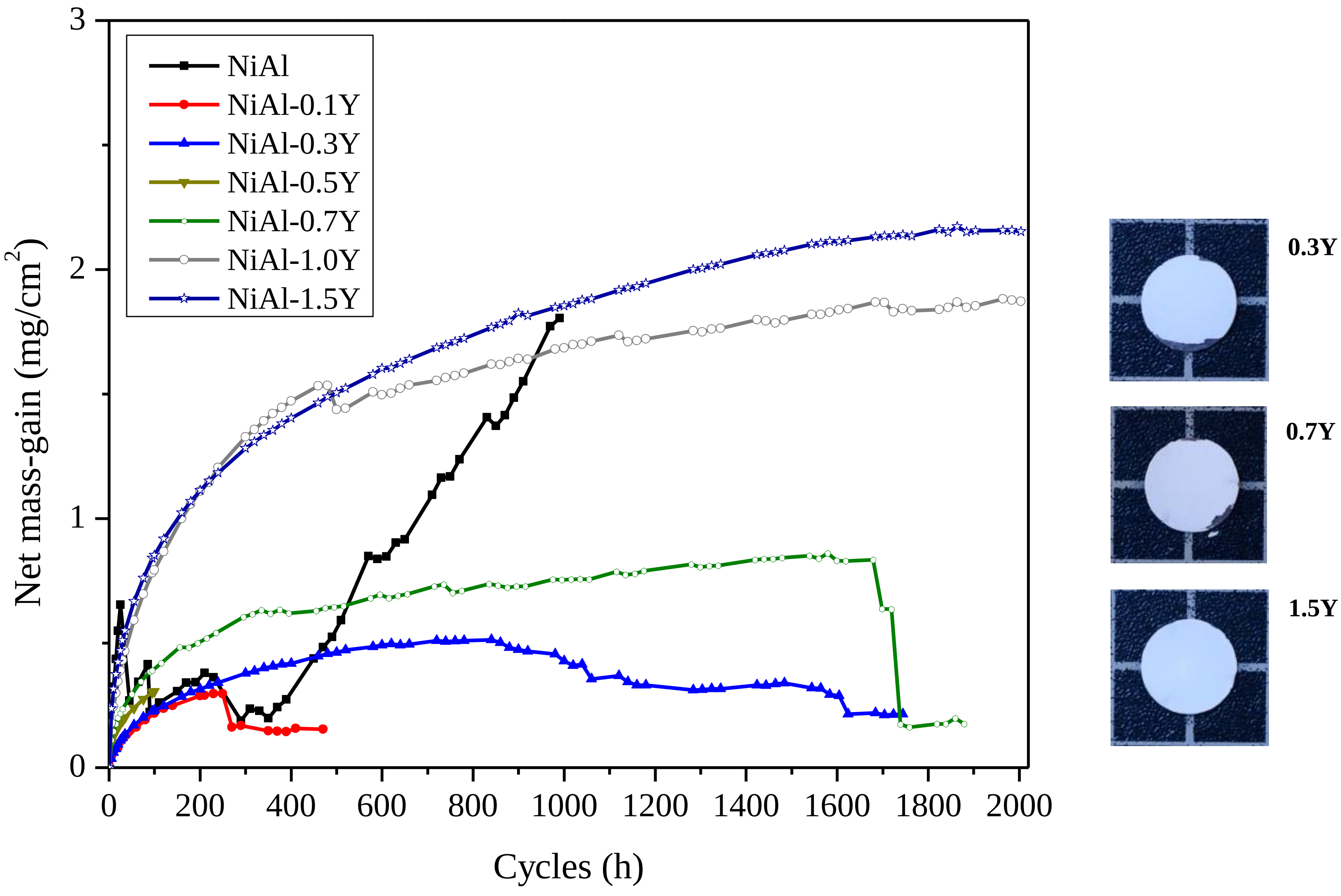

Muñoz Saldaña *et al.*

Figure 9

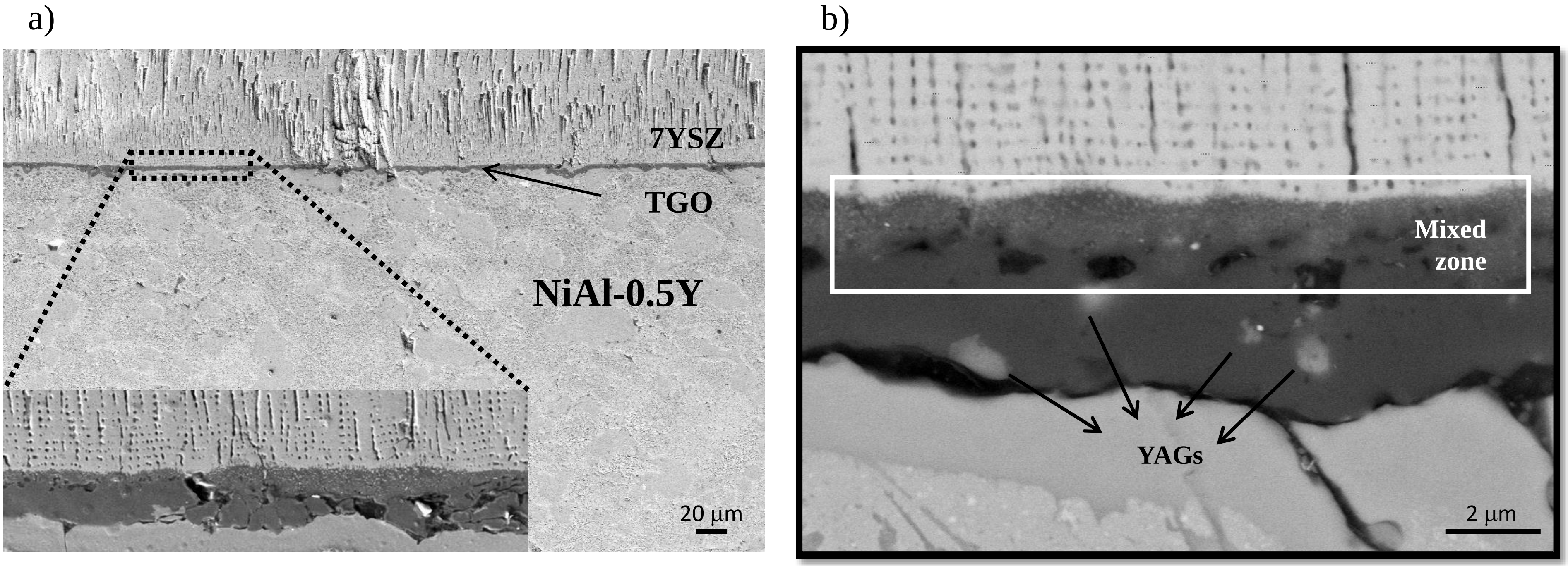

Muñoz Saldaña *et al.*

Table 1

ID	**Ni (at.%)**	**Al (at.%)**	**Y (at.%)**
NiAl_0.1Y	49.95	49.95	0.10
NiAl_0.3Y	49.85	49.85	0.30
NiAl_0.5Y	49.75	49.75	0.50
NiAl_1Y	49.50	49.50	1.00
NiAl_1.5Y	49.25	49.25	1.50

Table 2

Starting Powder	**Size distribution (μm)**			**Lattice parameter (Å)**	
	d_{10}	d_{50}	d_{90}	Theoretical	Calculated
Ni	71.90	93.09	110.81	$a = 3.523$	$a = 3.527 \pm 0.003$
Al	78.89	158.73	273.35	$a = 4.049$	$a = 4.048 \pm 0.002$
Y	10.68	56.55	225.42	$a = b = 3.647$ $c = 5.728$	$a = b = 3.668 \pm 0.005$ $c = 5.807 \pm 0.007$

Table 3

Number of balls	**BPR 10:1**		**BPR 6:1**		**BPR 4:1**	
	S	*a* (Å)	*S*	*a* (Å)	*S*	*a* (Å)
2	0.91	2.881 ± 0.004	0.97	2.883 ± 0.003	1.0	2.885 ± 0.002
3	0.86	2.886 ± 0.003	0.96	2.886 ± 0.003	0.84	2.883 ± 0.003
5	0.87	2.883 ± 0.005	0.85	2.890 ± 0.003	--	--

Table 4

Y content (at.%)	Lattice Parameter (Å)	Ordering parameter SPS buttons
0.0	2.886 ± 0.003	0.96
0.1	2.886 ± 0.001	0.81
0.3	2.888 ± 0.002	0.79
0.5	2.892 ± 0.002	0.82
1.0	2.893 ± 0.002	0.84
1.5	2.893 ± 0.003	0.85

Table 5

Y content (at.%)	***kp*** **($mg^2\ cm^{-4}\ s^{-1}$) TGA**	***kp*** **($mg^2\ cm^{-4}\ s^{-1}$) FCT**
0.0	1.02E-5 (after 6h)	**--**
0.1	--	**--**
0.3	1.15E-6	1.68E-7
0.5	2E-6	2.01E-7
1.0	1.12E-5	1.83E-6
1.5	1.96E-5	1.69E-6

Credit author statement

J. Muñoz-Saldaña: Conceptualization, Supervision, Resources, Methodology, Writing - Review & Editing, funding acquisition. **A. Valencia-Ramirez**: Investigation, Methodology, Data curation, Writing- Original draft preparation. **L.A Castillo-Perea:** Investigation, Methodology, Data curation. **S. Díaz-De la Torre**: Methodology. ***L.A. Caceres-Diaz****:* Formal Analysis, Review & Editing.**:** **J. M. Alvarado Orozco**: Formal Analysis, Review & Editing: **A. L. Giraldo Betancur:** Formal Analysis, Review & Editing. **U. Schulz**: Supervision, Resources, Writing - Review & Editing.

Declaration of interests

☒The authors declare that they have no known competing financial interests or personal relationships that could have appeared to influence the work reported in this paper.

☐The authors declare the following financial interests/personal relationships which may be considered as potential competing interests: